

# Combined Machine Learning and CALPHAD Approach for Discovering Processing-Structure Relationships in Soft Magnetic Alloys

Rajesh Jha<sup>a,\*</sup>, Nirupam Chakraborti<sup>b</sup>, David R. Diercks<sup>c</sup>, Aaron P. Stebner<sup>a</sup>, Cristian V. Ciobanu<sup>a,\*</sup>

<sup>a</sup>Department of Mechanical Engineering, Colorado School of Mines, Golden, Colorado 80401, USA

<sup>b</sup>Department of Metallurgical and Materials Engineering, Indian Institute of Technology Kharagpur, West Bengal, India

<sup>c</sup>Department of Metallurgical and Materials Engineering, Colorado School of Mines, Golden, Colorado 80401, USA

## Abstract

FINEMET alloys have desirable soft magnetic properties due to the presence of Fe<sub>3</sub>Si nanocrystals with specific size and volume fraction. To guide future design of these alloys, we investigate relationships between select processing parameters (composition, temperature, annealing time) and structural parameters (mean radius and volume fraction) of the Fe<sub>3</sub>Si domains. We present a combined CALPHAD and machine learning approach leading to well-calibrated metamodelling able to predict structural parameters quickly and accurately for any desired inputs. To generate data, we have used a known precipitation model to perform annealing simulations at a several temperatures, for varying Fe and Si concentrations. Thereafter, we used the data to develop metamodelling for mean radius and volume fraction via the *k*-Nearest Neighbour algorithm. The metamodelling reproduce closely the results from the precipitation model over the entire annealing timescale. Our analysis via parallel coordinate charts shows the effect of composition, temperature, and annealing time, and helps identify combinations thereof that lead to the desired mean radius and volume fraction for nanocrystals. This work contributes to understanding the linkages between processing parameters and desired microstructural characteristics responsible for achieving targeted properties, and illustrates ways to reduce the time from alloy discovery to deployment.

**Keywords:** Soft magnetic alloys, FINEMET, CALPHAD, Machine Learning, *k*-Nearest Neighbour Algorithm, Parallel Coordinate Chart

## 1. INTRODUCTION

FINEMET alloys belong to a class of soft magnetic alloys based on the Fe-Si-Nb-B-Cu system.<sup>1</sup> In comparison with other soft magnets, FINEMET alloys possess high saturation magnetization<sup>1</sup> and high permeability,<sup>2–5</sup> low core loss,<sup>1–3,5</sup> low magnetostriction,<sup>1–3,5,6</sup> excellent temperature characteristics, small aging effects, and excellent high frequency characteristics.<sup>1–3,5</sup> As a result, FINEMET alloys have been successfully used in a number of applications including choke coils,<sup>1,2,7–9</sup> mobile phones,<sup>2</sup> noise reduction devices,<sup>2</sup> computer hard disks,<sup>2</sup> and transformers.<sup>1–3,8,9</sup> Superior soft magnetic properties are attributed to the nanocrystalline  $\alpha''$ -(Fe, Si) phase (Fe<sub>3</sub>Si with D03 structure) in the size range of 10–15 nm diameter (radius 5–7.5 nm) and 0.7 volume fraction.<sup>1–6,8–16</sup> Since its discovery, researchers have investigated FINEMET alloys to improve upon multiple soft magnetic properties by performing experiments followed by characterization using advanced diagnostic tools.<sup>2,4,5,8,10–12,14–16</sup>

In materials design, understanding the various processing-structure-property (PSP) linkages plays an important role in designing advanced materials. In particular, correlations between microstructure and desired properties,<sup>17–20</sup> are essential for the deployment of new materials into service. In addition, composition variations and processing parameters (e.g., heat treatment schedule) play an integral role in modeling the microstructure(s) responsible for achieving desired properties, where optimizing processing parameters along with composition remains a challenging task.<sup>21</sup> As an alternative to costly experimentation, the CALPHAD approach allows for investigating the effect of composition variations and heat treatment on the size distribution and volume fraction of the phase(s) that are responsible for optimal or desired properties; indeed, it has been used for studying soft magnets containing amorphous phases<sup>22–24</sup> using the commercial software Thermocalc.<sup>25</sup> Recent studies indicate that simulations based on CALPHAD<sup>26,27</sup> are in need of efficiency improvements if they are to be used for optimization of the composition and heat treatment schedule. To address this challenge, it is important to develop models that can both replicate maximum information available from prior studies and, in addition,

\*Corresponding author

Email addresses: rajeshjha@mines.edu (Rajesh Jha), cciobanu@mines.edu (Cristian V. Ciobanu)

demonstrate effectiveness in optimizing the processing protocol. This effectiveness should not come, for example, from repeating the same calculations at different compositions, but rather from learning the results obtained in several selected cases in order to predict the behaviour at other compositions.

Machine learning approaches have been previously used to help reduce the time required in the alloy design process.<sup>28–38</sup> Supervised machine learning approaches such as artificial neural networks,<sup>37–40</sup>  $k$ -Nearest Neighbour algorithm ( $k$ -NN),<sup>38,41</sup> genetic programming,<sup>37,38,40,42</sup> kriging,<sup>43,44</sup> and unsupervised approaches such as Principal Component Analysis (PCA),<sup>30,31,35</sup> Hierarchical Clustering Analysis (HCA),<sup>29,31,34</sup> and Self Organizing Maps (SOM)<sup>28</sup> have been previously used in materials science and can also be helpful in this case. From an implementation point of view, there exist several open-source software packages to develop response surfaces or metamodels using several different concepts from artificial intelligence. A machine learning model based on results from the CALPHAD approach will serve as an important rapid screening tool before performing experiments and also in predicting outcomes in case of uncertainties in the composition of the material or in furnace temperature during annealing.

In this article, we present a combined CALPHAD-machine learning approach for optimizing composition along with processing parameters for FINEMET alloys by developing metamodels (response surfaces, or surrogate models) for the simulated crystallization of  $\text{Fe}_3\text{Si}$  domains. We have acquired data for mean radius and volume fraction of  $\text{Fe}_3\text{Si}$  nanocrystals through a recently developed precipitation model<sup>45</sup> in Thermocalc,<sup>25</sup> capable of simulating the nucleation and growth of  $\text{Fe}_3\text{Si}$  nanocrystals from an amorphous phase. Thereafter, we have used a  $k$ -Nearest Neighbour ( $k$ -NN) algorithm to generate computationally inexpensive metamodels to replace exhaustive Thermocalc modeling without any significant loss of accuracy. This way, we are able to demonstrate the efficacy of our combined CALPHAD-machine learning approach by predicting compositions and processing parameters that would lead to achieving the desired mean radius and volume fraction of  $\text{Fe}_3\text{Si}$  nanocrystals. The developed metamodels capture the established nucleation and growth evolution<sup>46,47</sup> within the CALPHAD approach, for the entire annealing timescale even for compositions and parameters that were not included in the training set for the metamodels. Another important observation is that the metamodels can predict outcomes in a fraction of the time taken by simulations in Thermocalc.<sup>48</sup> Lastly, we propose Parallel Coordinates Charts (PCC)<sup>49</sup> for comprehensive visualization of the relationships between processing parameters and optimized quantities, and for rapid identification of the parameters that lead to crystallization of

$\text{Fe}_3\text{Si}$  nanocrystals in the desired size range and volume fraction. Our proposed approach helps reduce the alloy development time since it can serve as a tool for rapid screening of the multi-dimensional parameter space before performing experiments. As such, this combined machine learning and CALPHAD approach illustrates a case of addressing the challenge of simultaneously determining the effect of composition variation and processing parameters<sup>17–21</sup> on the microstructure and can be extended to other alloy systems.

## 2. METHODS

Figure 1 shows the schematic flowchart of the process we followed in order to develop our combined CALPHAD-machine learning approach for optimization of nanocrystal size and volume fraction. This approach is enabled by a nucleation and growth model (precipitation model) in Thermocalc,<sup>50</sup> recently parameterized for FINEMET.<sup>45</sup> We used this model to generate data for mean radius and volume fraction of  $\text{Fe}_3\text{Si}$  nanocrystals grown upon annealing the amorphous material, data which serves as a training set for developing metamodels. Analysis of the results created by the metamodels reveals correlations between the input parameters (composition, temperature, and time) and the optimized quantities. The three aspects (Figure 1) are described in some detail below.

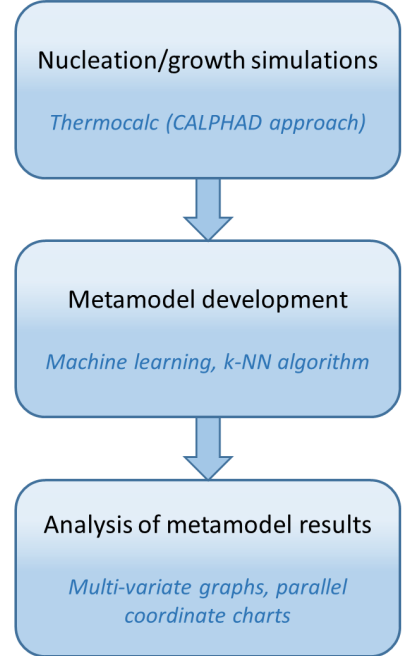


Figure 1: Flowchart of steps followed in this work for a class of FINEMET alloy with composition  $\text{Fe}_{72.89}\text{Si}_{16.21}\text{B}_{6.9}\text{Nb}_3\text{Cu}_1$

### 2.1. Generating data for developing a metamodel

To generate mean radius and volume fraction data,<sup>55</sup> we have used the TC-PRISMA<sup>50</sup> module in Thermocalc, which relies on thermodynamic (TCFE8)<sup>48</sup>

and mobility<sup>51</sup> databases. TC-PRISMA<sup>50</sup> uses the Kampmann-Wagner Numerical (KWN) method<sup>46,47</sup> for simulating nucleation and growth of precipitates during annealing. The KWN method is an extension of the Langer-Schwartz approach<sup>52</sup> and its modified form.<sup>53</sup> To use the precipitation model, several input quantities in TC-PRISMA<sup>50</sup> were previously parameterized<sup>45</sup> so that the precipitation model simulates specifically and accurately the nucleation and growth of Fe<sub>3</sub>Si nanocrystals during annealing. The FINEMET base composition is Fe<sub>82.35</sub>Si<sub>9.21</sub>B<sub>1.51</sub>Nb<sub>5.64</sub>Cu<sub>1.29</sub> in weight %, or Fe<sub>72.89</sub>Si<sub>16.21</sub>B<sub>6.90</sub>Nb<sub>3</sub>Cu<sub>1</sub> in atomic %; we will refer only to the latter in the remainder of the article. Simulations of precipitation were performed for new compositions Fe<sub>72.89+x</sub>Si<sub>16.21-x</sub>B<sub>6.90</sub>Nb<sub>3</sub>Cu<sub>1</sub> generated by varying the content of Fe and Si by  $x$  ( $-3 \leq x \leq 3$ ). Isothermal annealing was carried out at a set of temperatures between 490 °C and 550 °C in (increments of 10 °C) to for up to 2 hrs holding time. We obtained significant amounts of Thermocalc data for mean radius and volume fraction of Fe<sub>3</sub>Si nanocrystals,<sup>55</sup> which serves as training set for the machine learning stage of the workflow (Figure 1).

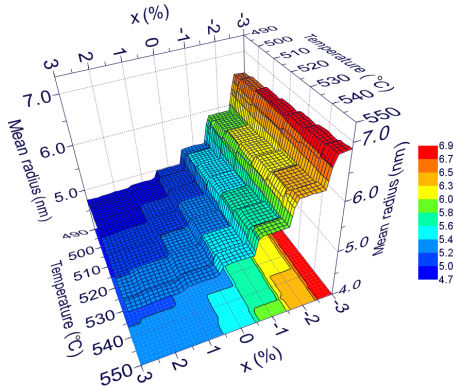


Figure 2: Mean radius of Fe<sub>3</sub>Si nanocrystals as a function of  $x$  and annealing temperature, for a holding time of 1 h.<sup>55</sup>

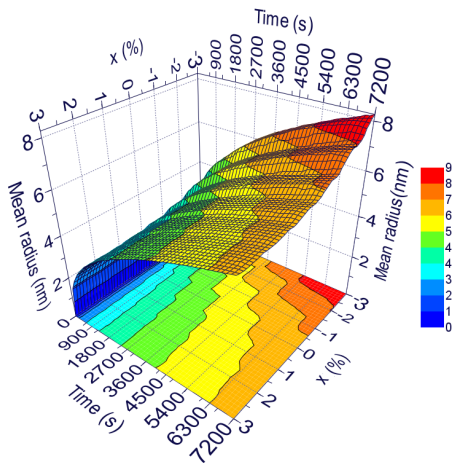


Figure 3: Mean radius of Fe<sub>3</sub>Si nanocrystals as a function of  $x$  and holding time, for a temperature of 500 °C.<sup>55</sup>

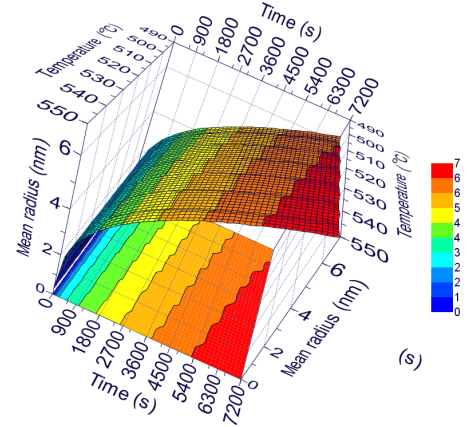


Figure 4: Mean radius of Fe<sub>3</sub>Si nanocrystals as a function of annealing temperature and holding time, for the nominal composition ( $x = 0$ ).<sup>55</sup>

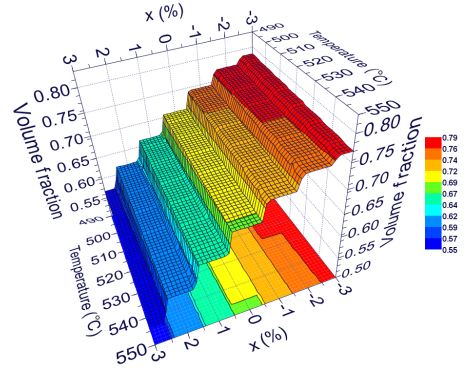


Figure 5: Volume fraction of Fe<sub>3</sub>Si nanocrystals as a function of annealing temperature and  $x$ , for 2 h holding time.<sup>55</sup>

## 2.2. $k$ -Nearest Neighbour Algorithm

The mean radius and volume fraction were generated in order to be used for creating response surfaces or metamodels to help in the design of future nanocrystalline FINEMET alloys. We use the  $k$ -NN algorithm<sup>41</sup> as implemented in the software modeFRONTIER<sup>54</sup> to construct the metamodels. This algorithm stores all the available information and predicts a new output (in this case, mean radius and volume fraction) based on a measure of similarity (distance function) of the new input with the stored cases. Specifically, to predict the new target/output that corresponds to a new input, the straightforward approach is to compute the average of the outputs of the first  $k$  nearest neighbors of the new input. In general, the average is weighted so that some neighbors contribute more to the average than others. In our work, we use  $k = 11$  neighbors for the metamodel describing the mean radius and volume fraction of Fe<sub>3</sub>Si nanocrystals as functions of  $x$ , annealing temperature, and holding time.

## 2.3. Parallel coordinates chart

A Parallel Coordinates Chart (PCC)<sup>49</sup> is a powerful tool used for visualizing large and multivariate sets

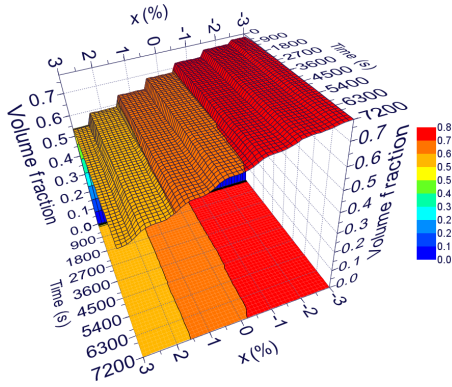


Figure 6: Volume fraction of  $\text{Fe}_3\text{Si}$  nanocrystals as a function of holding time and  $x$ , at a temperature of  $550^\circ\text{C}$ .<sup>55</sup>

of data or results.<sup>49</sup> It has been successfully implemented in applications such as visual and automatic data mining, optimization, decision support, and approximations.<sup>49</sup> We find it useful to apply PCCs to materials design as well, as a tool to visualize connections between the processing parameters and optimized quantities. In PCC, a number of parallel (vertical) coordinate axes represent the  $n$  dimensions of a given set of data. Any particular data point in the  $n$ -dimensional space is represented by a line that connects single points on each of the  $n$  parallel coordinate axes.

We have five parallel coordinate axes in this work, three variable (input) axes,  $x$ , temperature, holding time, and two function (output) axes, mean radius and volume fraction. Significant amounts of data were created, i.e., 22,000 data sets generated from the precipitation model and 22,000 sets generated through the metamodel for (new) randomly generated sets of variables ( $x$ , temperature, and time).<sup>55</sup> In order to properly explore the variable space, we used the Sobol algorithm<sup>56</sup> for sampling the  $x$ , temperature, and time domains. We analyzed all data using PCC to find the parameters that should be followed (or avoided) so as to crystallize  $\text{Fe}_3\text{Si}$  nanocrystals in the desired range for mean radius (5-7.5 nm) and volume fraction ( $> 0.7$ ). Another reason was to explore the possibility of decreasing holding time during isothermal annealing without compromising on size range and volume fraction.

### 3. RESULTS AND DISCUSSION

#### 3.1. Analysis of training set results and of the metamodel

Using the data obtained from Thermocalc for few compositions and temperatures, we plot the mean radius and volume fraction as surface meshes in which one of the variables ( $x$ , temperature, or time) is fixed at a certain value, while the other two are allowed to vary over their respective ranges (Figures 2–6). In

these mesh plots, surfaces appear stepped because they represent the training set in which  $x$  and temperature each vary in seven discrete, large steps. Even without a metamodel, these direct simulations show that one needs to avoid concentration deviations  $x > 0.5\%$  since they would not lead to mean radius in the desired range (Figure 2).

Using the metamodels based on the  $k$ -NN algorithm trained on data in Figures 2–6, we develop contour plots for mean radius and volume fraction as functions of temperature and  $x$ , for three annealing times (Figures 7, 8). In Figures 7 and 8, we show the 22,000 data sets that have not been used in the training of the  $k$ -NN metamodel. Other ways to plot the results from the metamodels so as to aid the design of the processing with ( $x$ , temperature, time) as variables and with two properties to optimize (radius and volume fraction) will be shown in Sec. 3.4.

Next, we focus on assessing the performance of the metamodels derived trained on the data in Figures 2–6).

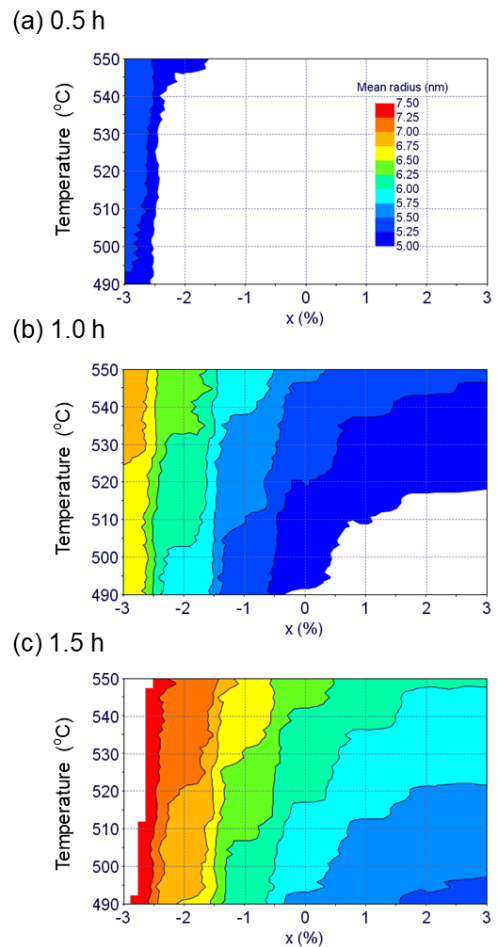


Figure 7: Mean radius predicted from the metamodel after (a) 0.5 h, (b) 1.0 h, and (c) 1.5 h annealing time. Only the desired values (5 – 7.5 nm) are shown in the contour plots.<sup>55</sup>

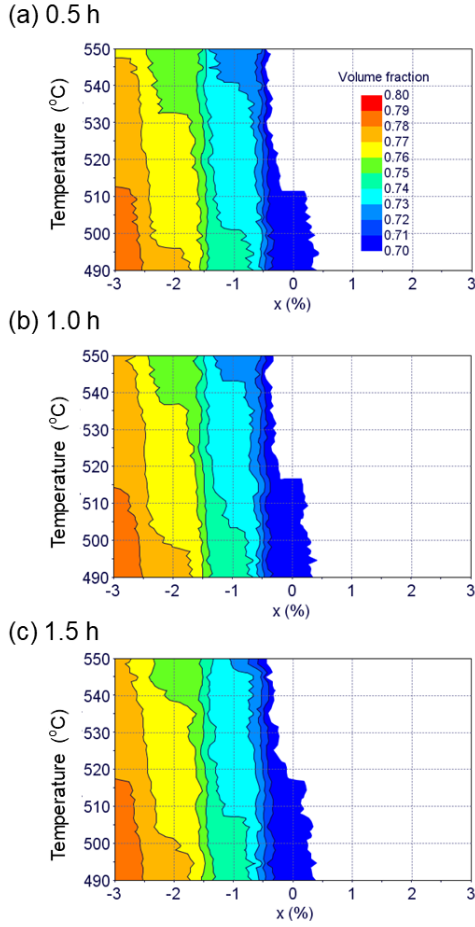


Figure 8: Volume fraction of the nanocrystalline phase predicted from the metamodel after (a) 0.5 h, (b) 1.0 h, and (c) 1.5 h annealing time. Only the desired values ( $\geq 0.7$ ) are shown in the contour plots.<sup>55</sup>

### 3.2. Predictions of the metamodel on Sobol sequences

To assess the usefulness of the metamodel for design, we compared its predictions for inputs that were not included in the training set, with Thermocalc results for the same new inputs. To sample the three-variable space, we use Sobol sequences<sup>56</sup> to generate 20,160 new random data input points for the three processing parameters as follows: 140 points for  $x$  between -3% and 3%, 12 points for temperatures between 490 and 550 °C, and 12 points for annealing times up to 2 h.

To illustrate comparisons between the predictions of the metamodel and direct Thermocalc results for the new 20,160 input data based on Sobol sequences and not used in the training set, we have selected three pairs of processing parameters, ( $x = 0.75$ , 515 °C), ( $x = 0$ , 515 °C) and ( $x = -2.95$ , 545 °C). Figure 9 and 10 show both the metamodel predictions (curves) and the Thermocalc calculations (dots) for the mean radius of  $\text{Fe}_3\text{Si}$  nanocrystals and their volume fraction, respectively. As apparent from these figures, there are only small deviations of the predictions of the metamodel from the direct Thermocalc results for the entire annealing duration considered. Referring to the 3D surface plots

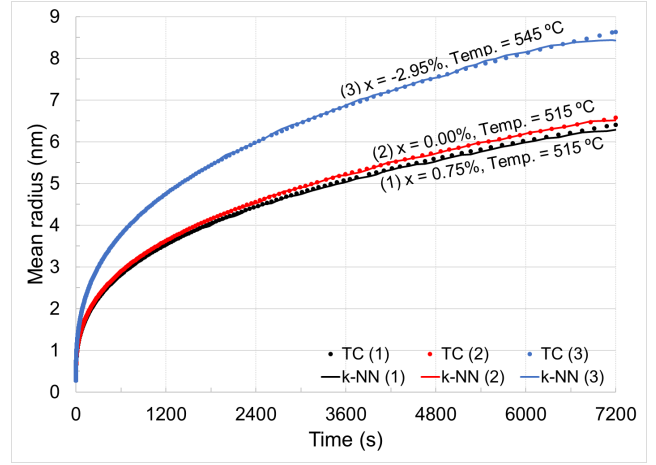


Figure 9: Mean radius ( $\text{Fe}_3\text{Si}$ ) vs. Time: Comparison between Thermocalc (TC) and metamodel (KN) prediction.<sup>55</sup>

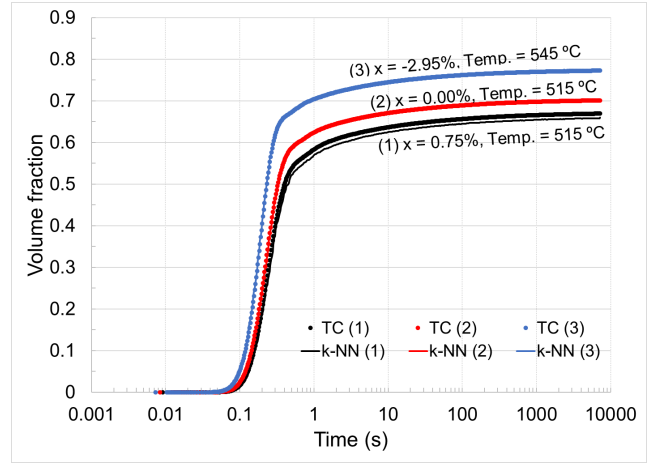


Figure 10: Volume fraction( $\text{Fe}_3\text{Si}$ ) vs. Time: Comparison between Thermocalc (TC) and metamodel (KN) prediction.<sup>55</sup>

(Figures 2–6), we mentioned that their stepped appearance was due to the sparseness of the training sets for temperature and composition deviation  $x$ . Despite the sparseness of the training data, we note that the developed response surfaces (metamodels) are able to capture closely the trends observed during nucleation and growth of  $\text{Fe}_3\text{Si}$  nanocrystals for both mean radius (Figure 9) and volume fraction (Figure 10), even though the machine learning algorithm was not exposed to the physical principles of nucleation and growth: this illustrates the predictive power of the machine learning approach in this case. Next, we will show quantitative assessments of the accuracy of the model trained on different subsets of the original 24,000 datapoint training set.

### 3.3. Assessment of the prediction accuracy for the metamodel on different training sets

In order to assess quantitatively the accuracy of the predictions of the metamodel, we have divided the initial 24,000 data sets into 90%-10% partitions (splits),

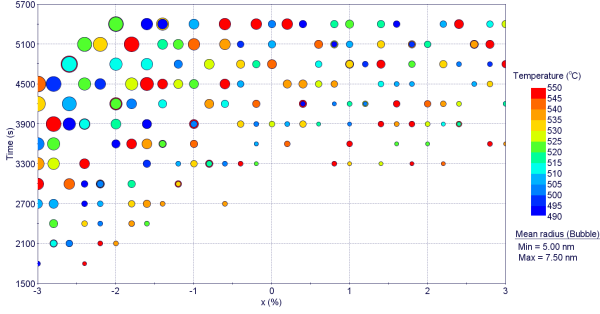


Figure 11: Mean radius (circles) for different values of  $x$ , annealing time, and temperature. For clarity, only a subset of 300 data sets is shown.<sup>55</sup>

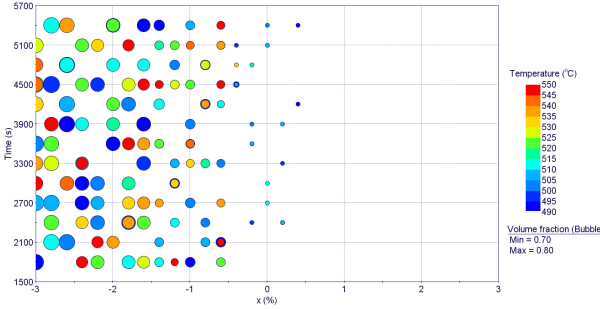


Figure 12: Volume fraction for different values of  $x$ , annealing time, and temperature. To avoid overlaps, only a subset of 300 data sets is shown.<sup>55</sup>

in which 90% of the set (21,600 datasets) are used for training, and the remaining (unseen) 2,400 points are used for testing the accuracy. We have created 20 such disjointed, random splits ( $j = 1, 2, \dots, 20$ ), each of which containing a set of unseen inputs  $\mathbf{x}_{i_j}$ , where the index  $i_j = 1, 2, \dots, 2,400$  counts the testing data in split  $j$  and the vector  $\mathbf{x}$  denotes the triplet ( $x$ , temperature, time). Since both the mean radius  $R$  and the volume fraction  $f$  vary from near zero to a finite quantity during nucleation and growth, we calculate the percent relative error (rather than the absolute error),

$$\varepsilon_{R,i_j}^{(j)} = 100 \frac{|R_{\text{pred}}(\mathbf{x}_{i_j}) - R_{\text{act}}(\mathbf{x}_{i_j})|}{R_{\text{act}}(\mathbf{x}_{i_j})}, \quad (1)$$

where the superscript  $(j)$  indicates the split index, and the subscripts “pred” and “act” refer to the prediction of the metamodel trained on the training set  $j$  and the actual value computed by Thermocalc, respectively. Similarly, the error for the volume fraction  $f$  is computed as

$$\varepsilon_{f,i_j}^{(j)} = 100 \frac{|f_{\text{pred}}(\mathbf{x}_{i_j}) - f_{\text{act}}(\mathbf{x}_{i_j})|}{f_{\text{act}}(\mathbf{x}_{i_j})}. \quad (2)$$

For each split  $j = 1, 2, \dots, 20$ , we determine the minimum, maximum, average, and 95 percentile error and tabulate the results (Tables 1 and 2). Furthermore, we compute the average and standard deviations of each of these errors across all the splits, and list these in the last two rows of Table 1 and 2; for example,  $\varepsilon_R$  and

$\sigma_R$  for the “avrg.” column in Table 1 are defined, respectively, as the average and standard deviation of the average errors corresponding to the 20 splits.

We note that, overall, the accuracy of the model is very good since it yield errors almost always are within less than 1% from the Thermocalc-computed mean radius and volume fraction (exact values of the different types of error measures are listed in Tables 1 and 2). The results in the maximum error column of Table 2 may at first sight appear alarming, since they show maximum relative errors between 8 and 13%. Upon closer inspection of the data, we have determined that the points responsible for these types of large (maximum) relative errors correspond to annealing times of the order of seconds: for such small timeframes, the volume fractions are very close to zero so any deviation from the (small) Thermocalc values  $f_{\text{act}}(\mathbf{x}_{i_j})$  could trigger a large relative error via Eq. (2). Indeed, when considering the entire 2,400 datasets in any of the testing partitions  $j$ , the average error is smaller than (1/3) of a percent (Table 2). This problem does not appear for the mean radius because  $R$  (Table 1) increases abruptly from zero, while the volume fraction has nearly zero derivative at the onset (10).

Table 1: Relative error (%) for mean radius for the testing set of each of the 20 different random, disjointed splits of the 24,000 datasets into 90% training and 10% testing.

$j$	Relative error (%) for mean radius			
	min.	max.	avrg.	95 perc.
1	6.3E-06	1.843	0.152	0.498
2	4.8E-05	1.429	0.147	0.473
3	2.5E-06	1.180	0.149	0.485
4	1.6E-04	1.935	0.147	0.471
5	6.0E-06	1.187	0.145	0.472
6	9.3E-05	1.440	0.147	0.479
7	6.8E-05	1.214	0.146	0.475
8	1.9E-05	1.130	0.153	0.517
9	1.0E-06	1.078	0.142	0.475
10	7.0E-05	1.592	0.150	0.484
11	5.9E-05	3.138	0.154	0.498
12	6.0E-06	1.052	0.145	0.483
13	9.6E-05	1.649	0.152	0.509
14	6.0E-05	0.925	0.149	0.510
15	2.4E-04	1.800	0.151	0.487
16	4.0E-06	1.462	0.152	0.495
17	7.0E-06	2.079	0.152	0.486
18	4.3E-05	1.289	0.147	0.493
19	3.9E-05	1.480	0.153	0.517
20	6.0E-06	1.341	0.146	0.483
$\varepsilon_R$	5.2E-05	1.512	0.149	0.490
$\sigma_R$	6.1E-05	0.495	0.003	0.015

We have tested many other sets of input parameter sets as well, and have concluded that the metamodel developed via the  $k$ -Nearest Neighbour algorithm is sufficiently robust that its predictions can be verified

Table 2: Relative error (%) for volume fraction for the testing set of each of the 20 different random, disjointed splits of the 24,000 datasets into 90% training and 10% testing.

$j$	Relative error (%) for volume fraction			
	min.	max.	avrg.	95 perc.
1	1.2E-05	11.532	0.227	1.190
2	1.5E-05	10.21	0.203	1.136
3	7.4E-06	8.600	0.178	0.778
4	2.0E-06	14.63	0.221	1.106
5	8.4E-06	9.71	0.199	1.006
6	8.5E-06	6.58	0.135	0.630
7	6.9E-07	15.30	0.182	0.891
8	4.1E-06	8.95	0.162	0.709
9	9.9E-06	11.04	0.195	0.889
10	9.7E-06	8.30	0.182	0.897
11	2.3E-05	9.99	0.157	0.810
12	2.3E-06	9.38	0.185	0.879
13	8.6E-06	11.06	0.148	0.678
14	1.8E-05	10.60	0.205	1.078
15	5.0E-06	12.09	0.196	0.871
16	1.3E-06	9.53	0.199	1.057
17	1.0E-05	12.56	0.266	1.379
18	7.4E-06	11.96	0.188	0.755
19	1.2E-05	11.52	0.228	1.294
20	2.0E-06	8.93	0.190	0.985
$\varepsilon_f$	8.4E-06	10.62	0.192	0.951
$\sigma_f$	5.9E-06	2.09	0.030	0.204

back and forth for random compositions and processing parameters. Lastly, in order to emphasize the potential usefulness of the metamodel for design purposes, we have estimate the time taken by the metamodel to drive experimental predictions for different processing parameters. Table 3 shows a comparison of time estimates for experiments (annealing estimated at 1 h per sample at a given temperature), direct CALPHAD calculations, and the metamodel: as seen in Table 3, for large numbers of datasets (44,000) the time decreases from years (experiments) to minutes (metamodel). In practice, the experiments simply would not be performed for such large datasets and researchers would necessarily have to make inferences from far fewer sets of data. The availability of a metamodel in this case allows for the rapid identification of experimental conditions/parameters that lead to optimal mean radius and volume fraction.

### 3.4. Other representations of the metamodel results for use in multivariate design space

We note that contour plots such as those in Figures 7 and 8 do not fully show all of the information that practitioners may need. In particular, creating multiple time slices could make the use of the metamodels cumbersome. To further pursue the idea of charting the parameter space, we are pursuing graphical ways to represent all the correlations between the optimized quantities and the input parameters; in other

words, we develop graphical ways to show the predictions of the metamodel so as to facilitate their use for design purposes. One such way is to represent each optimized quantity (mean radius and volume fraction) in terms of all three inputs using “bubble” plots (Figures 11 and 12), in which the inputs are on the horizontal axis ( $x$ ), vertical axis (time), and on a color scale (temperature). For such representations, the mean radius or the volume fraction predicted by the metamodel are shown as circles of different radii (Figures 11, 12). Armed with an interactive plot (such as those created in modeFRONTIER), a practitioner seeking to design FINEMET alloys would choose a mean radius, and then simply read out from the bubble plots (Figure 11) various possibilities (i.e.,  $x$ , temperature, and time) leading to that mean radius. The value added by such plots is that they can supply multiple combinations of parameters for the same mean radius or volume fraction, thereby providing choices for experimentalists. For example, it can be beneficial or cost-effective to choose lower temperatures and shorter annealing times, which may be enabled by minor composition variations.

While such bubble plots show each optimized quantity for all the three inputs, one can encounter optimization problems with more than three inputs and more than two optimized quantities. We propose that, in general, all inputs and outputs can be shown on parallel coordinates, as mentioned in the Methods section. PCCs<sup>49</sup> are an effective way to demonstrate the relationships between desired properties (output) and the input parameters for high dimensional data, in which the inputs and outputs stand on equal footing: any input or output quantity is shown on one of the parallel axes. We can use PCCs to assess the effect of each separate input on the design quantities (Figure 13), or we can choose design targets and then select input parameters from the many sets that lead to that design target (Figures 14, 15).

Figures 13(a),(b), and (c) show the effect of  $x$ , temperature, and time, respectively on the mean radius and volume fractions. The same 44,000 data sets<sup>55</sup> were plotted in all three panels of Figure 13, with the difference that the color scale from red to blue is placed on the different input axes for ease of separating the individual effects on mean radius and volume fraction. Consistent with the other analysis (Figure 7), lowering the concentration deviation  $x$  (Figure 13(a)) increases the mean radius and the volume fraction. The effect of temperature is not so obvious from these PCCs with large amounts of data, since it is strongly coupled with the effect of annealing time. As such, all temperatures can lead to the desired range of mean radius and volume fraction, provided that the annealing time is greater than 0.5 h (Figures 13(b,c)). In practice, the PCC charts are interactive: a user can simply click select a line crossing the axis of a quantity to be op-

Table 3: Comparison of time estimates between experiments, CALPHAD, and machine learning approach.

Set of parameters	Average Annealing time		
	Experiments	CALPHAD (Thermocalc)	Machine Learning
1	1 hour	30 Seconds	Developing metamodel: Less than 2 Minutes
44,000	44,000 Hours = 1,833 Days = <b>5 Years (Just annealing)</b>	366 Hours = <b>15.28 Days</b>	Less than 2 minutes <b>Total: Less than 4 minutes.</b>

timized, and then the values for all the parallel coordinates are displayed: in particular, a large set of input triplets. For clarity, we illustrate this point here with a very small amount of (selected) data. For clarity, in Figure 14 we display only three such sets of input triplets corresponding to a selected mean radius of 6 nm. In this figure, the nominal composition requires 550 °C and annealing for 1.28 h (4600 s). Allowing the concentration to deviate from the nominal one (e.g.,  $x = -1.45\%$  or  $-2.25\%$ ) can lead to lowering both the temperature and the annealing duration (Figure 14). This is precisely the value that the metamodel brings to the design process, i.e. providing accurate, rapidly computed input parameters that guide the processing so as to obtain desired outputs (mean radius and volume fraction) while often allowing for time and cost optimizations as well. For completeness, we also present the PCCs with separate color scales for the two optimized properties (Figure 15).

#### 4. CONCLUSIONS

From the results of the metamodel, there are several general conclusions pertaining the effects of input parameters on mean radius and volume fraction. For short anneal times (0.5 h), nanocrystals with the desired mean radius can be achieved for any temperature in the range considered, provided that  $x < -2.5\%$ . When annealing is sufficiently long (2 h), then all compositions  $x$  investigated can lead to mean radius in the desired range. A volume fraction  $> 0.7$  can be obtained for all the investigated temperatures and for all holding times longer than 0.5 h, provided that the composition deviation  $x$  falls below the threshold of  $+0.5\%$ .

The metamodels provide not only general trends, but, more importantly, specific and multiple inputs that lead to the desired output (mean volume and volume fraction). These are important choices for design, which can be carried out based completely based on the metamodel simulation results. In particular, the PCCs would help practitioners decide the inputs based on their material composition and even on economic considerations (lower anneal temperature and/or time for large scale production).

The present results illustrate a robust approach for discovering relationships between processing and structure/morphology in nanocrystalline alloys. Taking a broader perspective view on these results, the combined CALPHAD-machine learning approach can be in principle generalized for many other design situations in which structure or morphology optimization via processing conditions is necessary. Key factors for obtaining predictive metamodels would be to ensure all important inputs are considered, and to judiciously select the machine learning technique based on with the characteristics of the training data available.

#### 5. ACKNOWLEDGMENTS

The authors acknowledge the financial support from the National Science Foundation through Grant. No. DMREF-1629026.

#### 6. Data Availability

Data created during this work, along with the corresponding figures, has been deposited to the repository maintained by Citrine Informatics; files are available for public access<sup>55</sup> at <https://citrine.com/datasets/154863/>

#### References

- [1] Y. Yoshizawa, S. Oguma, K. Yamauchi, New fe-based soft magnetic alloys composed of ultrafine grain structure, *Journal of Applied Physics* 64 (1988) 6044–6046.
- [2] M. A. Willard, M. Daniil, Nanocrystalline soft magnetic alloys two decades of progress, *Handbook of Magnetic Materials* 21 (2013) 173–342.
- [3] G. Herzer, Chapter 3: Nanocrystalline soft magnetic alloys, Vol. 10 of *Handbook of Magnetic Materials*, Elsevier, 1997, pp. 415–462.
- [4] K. Hono, A. Inoue, T. Sakurai, Atom probe analysis of  $\text{Fe}_{73.5}\text{Si}_{13.5}\text{B}_9\text{Nb}_3\text{Cu}_1$  nanocrystalline soft magnetic material, *Applied Physics Letters* 58 (1991) 2180–2182.
- [5] H. Lashgari, D. Chu, S. Xie, H. Sun, M. Ferry, S. Li, Composition dependence of the microstructure and soft magnetic properties of fe-based amorphous/nanocrystalline alloys: A review study, *Journal of Non-Crystalline Solids* 391 (2014) 61–82.
- [6] N. Mattern, A. Danzig, M. Müller, Effect of Cu and Nb on crystallization and magnetic properties of amorphous  $\text{Fe}_{77.5}\text{Si}_{15.5}\text{B}_7$  alloys, *Materials Science and Engineering: A* 194 (1995) 77–85.

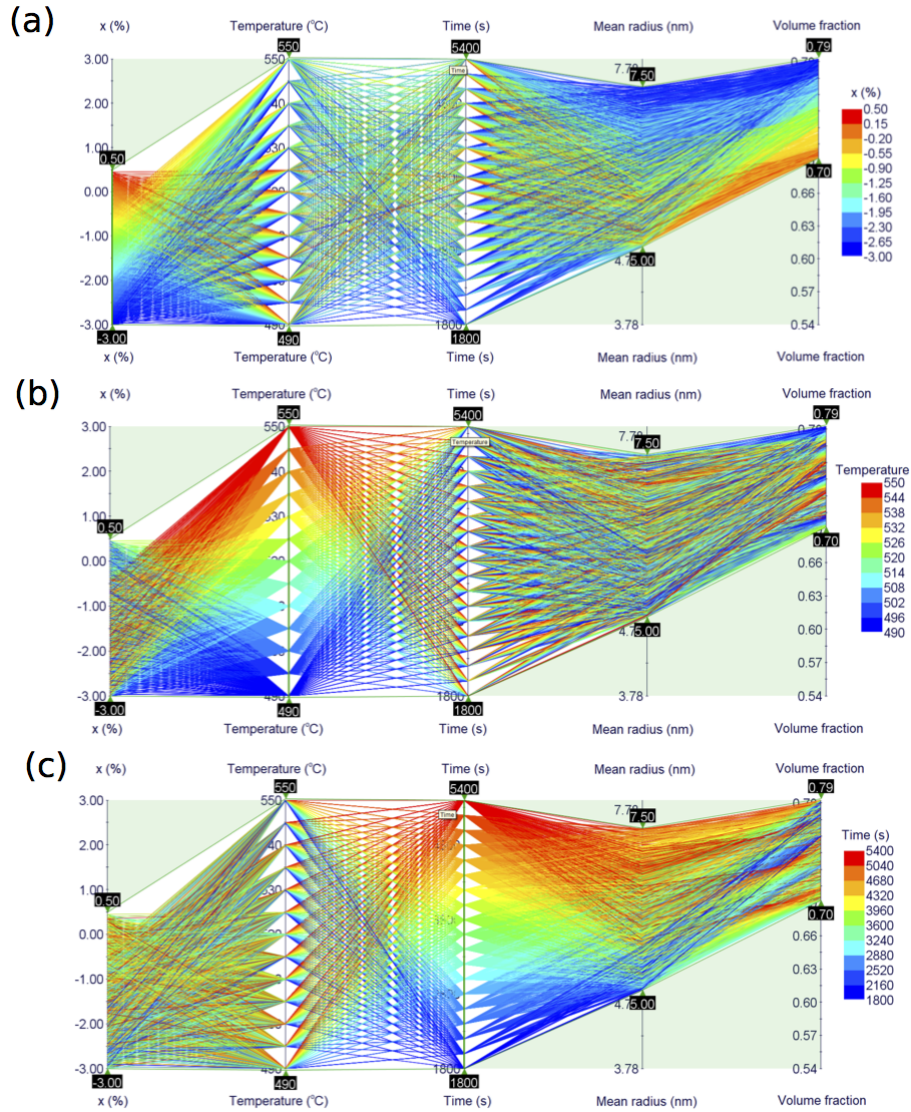


Figure 13: Parallel coordinates chart for input variables (a)  $x$ , (b) temperature, and (c) time from 44,000 sets of data.<sup>55</sup>

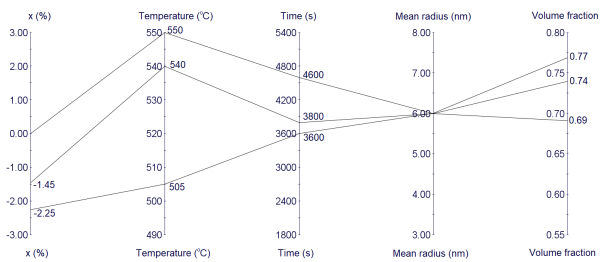


Figure 14: Parallel coordinates chart for mean radius of  $\text{Fe}_3\text{Si}$  nanocrystals. For clarity, this PCC shows only three of the ( $x$ , temperature, time) sets that lead to one desired mean radius (6 nm).<sup>55</sup>

- [7] M. E. McHenry, M. A. Willard, D. E. Laughlin, Amorphous and nanocrystalline materials for applications as soft magnets, *Progress in Materials Science* 44 (1999) 291 – 433.
- [8] G. Herzer, Nanocrystalline soft magnetic materials, *Physica Scripta* 1993 (1993) 307.
- [9] G. Herzer, Modern soft magnets: Amorphous and nanocrystalline materials, *Acta Materialia* 61 (2013) 718–734.

- [10] J. Ayers, V. Harris, J. Sprague, W. Elam, H. Jones, A model for nucleation of nanocrystals in the soft magnetic alloy  $\text{Fe}_{73.5}\text{Nb}_3\text{Cu}_1\text{Si}_{13.5}\text{B}_9$ , *Nanostructured Materials* 9 (1997) 391–396.
- [11] F. van Bouwelen, J. Sietsma, A. Van Den Beukel, Nb-driven nanocrystallization of amorphous  $\text{Fe}_{75.5}\text{Cu}_1\text{Nb}_3\text{Si}_{12.5}\text{B}_8$ , *Journal of non-crystalline solids* 156 (1993) 567–570.
- [12] G. Herzer, Magnetization process in nanocrystalline ferromagnets, *Materials Science and Engineering A* 133 (1991) 1–5.
- [13] G. Herzer, S. Flohrer, C. Polak, Effect of stress annealing on the saturation magnetostriction of nanocrystalline  $\text{Fe}_{73.5}\text{Cu}_1\text{Nb}_3\text{Si}_{15.5}\text{B}_7$ , *IEEE Transactions on Magnetics* 46 (2010) 341–344.
- [14] M. T. Clavaguera-Mora, N. Clavaguera, D. Crespo, T. Pradell, Crystallisation kinetics and microstructure development in metallic systems, *Progress in Materials Science* 47 (2002) 559–619.
- [15] C. Conde, A. Conde, Crystallization of a finemet-type alloy: nanocrystallization kinetics, *Materials Letters* 21 (1994) 409–414.
- [16] K. Hono, D. Ping, M. Ohnuma, H. Onodera, Cu clustering and si partitioning in the early crystallization stage of an  $\text{Fe}_{73.5}\text{Si}_{13.5}\text{B}_9\text{Nb}_3\text{Cu}_1$  amorphous alloy, *Acta materialia* 47

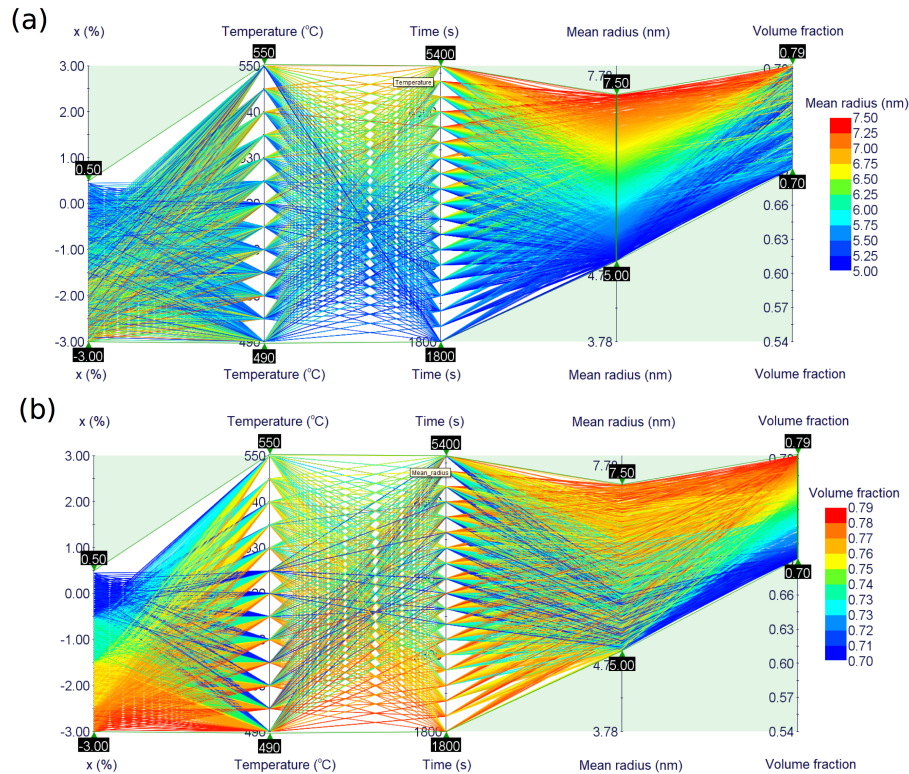


Figure 15: Parallel coordinates charts obtained from 44,000 sets of data for (a) mean radius and (b) volume fraction (separate color legends) of Fe<sub>3</sub>Si nanocrystals.<sup>55</sup>

(1999) 997–1006.

[17] A. Khosravani, A. Cecen, S. R. Kalidindi, Development of high throughput assays for establishing process-structure-property linkages in multiphase polycrystalline metals: Application to dual-phase steels, *Acta Materialia* 123 (2017) 55–69.

[18] E. Popova, T. M. Rodgers, X. Gong, A. Cecen, J. D. Madison, S. R. Kalidindi, Process-structure linkages using a data science approach: Application to simulated additive manufacturing data, *Integrating Materials and Manufacturing Innovation* 6 (2017) 54–68.

[19] N. H. Paulson, M. W. Priddy, D. L. McDowell, S. R. Kalidindi, Reduced-order structure-property linkages for polycrystalline microstructures based on 2-point statistics, *Acta Materialia* 129 (2017) 428–438.

[20] E. A. Pfeif, K. Kroenlein, Perspective: Data infrastructure for high throughput materials discovery, *APL Materials* 4 (2016) 053203.

[21] A. Agrawal, P. D. Deshpande, A. Cecen, G. P. Basavarsu, A. N. Choudhary, S. R. Kalidindi, Exploration of data science techniques to predict fatigue strength of steel from composition and processing parameters, *Integrating Materials and Manufacturing Innovation* 3 (2014) 8.

[22] A. Takeuchi, A. Makino, Thermodynamic assessment of fe-bp-cu nanocrystalline soft magnetic alloys for their crystallizations from amorphous phase, *Materials Transactions* 55 (2014) 1852–1858.

[23] A. Takeuchi, Y. Zhang, K. Takenaka, A. Makino, Thermodynamic analysis of binary Fe<sub>85</sub>B<sub>15</sub> to quinary Fe<sub>85</sub>Si<sub>2</sub>B<sub>8</sub>P<sub>4</sub>Cu<sub>1</sub> alloys for primary crystallizations of  $\alpha$ -Fe in nanocrystalline soft magnetic alloys, *Journal of Applied Physics* 117 (2015) 173737.

[24] T. Takahashi, K. Yoshida, Y. Shimizu, A. Setyawan, M. Bito, M. Abe, A. Makino, Fe-Si-B-P-C-Cu nanocrystalline soft magnetic powders with high  $B_s$  and low core loss, *AIP Advances* 7 (2017) 056111.

[25] THERMOCALC, Website (2017). URL <http://www.thermocalc.com/>

[26] H. Larsson, L. Höglund, A scheme for more efficient usage of calphad data in simulations, *Calphad* 50 (2015) 1–5.

[27] R. Pillai, T. Galiullin, A. Chyrkin, W. Quadackers, Methods to increase computational efficiency of calphad-based thermodynamic and kinetic models employed in describing high temperature material degradation, *Calphad* 53 (2016) 62–71.

[28] R. Jha, G. S. Dulikravich, N. Chakraborti, M. Fan, J. Schwartz, C. C. Koch, M. J. Colaco, C. Poloni, I. N. Egorov, Self-organizing maps for pattern recognition in design of alloys, *Materials and Manufacturing Processes* 32 (2017) 1067–1074.

[29] R. Jha, G. Dulikravich, M. Colaco, M. Fan, J. Schwartz, C. Koch, Magnetic alloys design using multi-objective optimization, in: *Properties and Characterization of Modern Materials*, Vol. 33, Springer Singapore, 2017, 261–284.

[30] R. Jha, G. S. Dulikravich, N. Chakraborti, M. Fan, J. Schwartz, C. C. Koch, M. J. Colaco, C. Poloni, I. N. Egorov, Algorithms for design optimization of chemistry of hard magnetic alloys using experimental data, *Journal of Alloys and Compounds* 682 (2016) 454–467.

[31] R. Jha, Combined computational-experimental design of high-temperature, high-intensity permanent magnetic alloys with minimal addition of rare-earth elements, Florida International University Electronic Theses and Dissertations, 2621.

[32] M. Fan, Y. Liu, R. Jha, G. S. Dulikravich, J. Schwartz, C. Koch, On the formation and evolution of Cu–Ni-rich bridges of AlNiCo alloys with thermomagnetic treatment, *IEEE Transactions on Magnetics* 52 (2016) 1–10.

[33] R. Jha, G. S. Dulikravich, M. J. Colaco, Design optimization of magnetic alloys and nickel-based superalloys for high temperature applications, in: *23rd ABCM International Congress of Mechanical Engineering - COBEM 2015, December 6-11 (2015)*, Rio de Janeiro, Brazil, ABCM International Congress of Mechanical Engineering, 2015.

[34] R. Jha, G. S. Dulikravich, M. J. Colaco, M. Fan, J. Schwartz,

- C. C. Koch, Magnetic alloys design using multi-objective optimization, in: ACE-X2015, June 29th - July 2nd (2015), Munich, Germany, 2015.
- [35] R. Jha, G. Dulikravich, N. Chakraborti, M. Fan, J. Schwartz, C. Koch, M. Colaco, Algorithms for multi-objective design optimization of hard magnetic alloys using experimental data, in: Proc. ICMM4, 2015, 1–19.
- [36] M. Fan, Y. Liu, R. Jha, G. S. Dulikravich, J. Schwartz, C. Koch, On the evolution of Cu-Ni-rich bridges of AlNiCo alloys with tempering, *Journal of Magnetism and Magnetic Materials* 420 (2016) 296–302.
- [37] R. Jha, F. Pettersson, G. Dulikravich, H. Saxen, N. Chakraborti, Evolutionary design of nickel-based superalloys using data-driven genetic algorithms and related strategies, *Materials and Manufacturing Processes* 30 (2015) 488–510.
- [38] R. Jha, G. S. Dulikravich, F. Pettersson, H. Saxen, N. Chakraborti, A combined experimental-computational approach to design optimization of high temperature alloys, in: ASME Symposium on Elevated Temperature Application of Materials for Fossil, Nuclear, and Petrochemical Industries, 2014.
- [39] F. Pettersson, N. Chakraborti, H. Saxén, A genetic algorithms based multi-objective neural net applied to noisy blast furnace data, *Applied Soft Computing* 7 (2007) 387–397.
- [40] R. Jha, P. K. Sen, N. Chakraborti, Multi-objective genetic algorithms and genetic programming models for minimizing input carbon rates in a blast furnace compared with a conventional analytic approach, *steel research international* (2) (2014) 219–232.
- [41] K.-N. N. Algorithm, K-nn (2017).  
URL <http://www.statsoft.com/Textbook/k-Nearest-Neighbors>
- [42] B. K. Giri, F. Pettersson, H. Saxén, N. Chakraborti, Genetic programming evolved through bi-objective genetic algorithms applied to a blast furnace, *Materials and Manufacturing Processes* 28 (2013) 776–782.
- [43] P. D. Pantula, S. S. Miriyala, K. Mitra, Kernel: Enabler to build smart surrogates for online optimization and knowledge discovery, *Materials and Manufacturing Processes* 32 (2017) 1162–1171.
- [44] T. Chugh, N. Chakraborti, K. Sindhya, Y. Jin, A data-driven surrogate-assisted evolutionary algorithm applied to a many-objective blast furnace optimization problem, *Materials and Manufacturing Processes* 32 (2017) 1172–1178.
- [45] R. Jha, D. Diercks, A. Stebner, C. V. Ciobanu, Metastable phase diagrams and precipitation kinetics of magnetic nanocrystals in finemet alloys, arXiv:1709.08306 [cond-mat.mtrl-sci].
- [46] R. Kampmann, R. Wagner, Decomposition of alloys: the early stages, in: Proc. 2nd Acta-Scripta Metall. Conf., Pergamon, Oxford, 1984, pp. 91–103.
- [47] R. Wagner, R. Kampmann, P. W. Voorhees, Homogeneous second-phase precipitation, *Materials science and technology*.
- [48] THERMOCALC, Tcfe8 database (2017).  
URL [http://www.thermocalc.com/media/10306/dbd\\_tcfe8\\_extendedinfo.pdf](http://www.thermocalc.com/media/10306/dbd_tcfe8_extendedinfo.pdf)
- [49] A. Inselberg, *Parallel Coordinates*, Springer New York, New York, NY, 2009, pp. 1–50. doi:10.1007/978-0-387-68628-8\_1.  
URL [https://doi.org/10.1007/978-0-387-68628-8\\_1](https://doi.org/10.1007/978-0-387-68628-8_1)
- [50] THERMOCALC, Tcprisma (2017).  
URL [http://www.thermocalc.com/media/46064/Precipitation-Module-TC-PRISMA-User-Guide\\_2016a.pdf](http://www.thermocalc.com/media/46064/Precipitation-Module-TC-PRISMA-User-Guide_2016a.pdf).
- [51] THERMOCALC, Tcfe8, mobfe3 database (2017).  
URL <http://www.thermocalc.com/media/32320/marketing-database-overview-oct-2016.pdf>
- [52] J. Langer, K. Schwartz, Kinetics of nucleation in near-critical fluids, *Physical Review A* 21 (1980) 948.
- [53] Computherm, Precipitation simulation (2017).  
URL [https://www.nist.gov/sites/default/files/documents/mml/msed/thermodynamics\\_kinetics/Precipitation-Simulation\\_CompuTherm.pdf](https://www.nist.gov/sites/default/files/documents/mml/msed/thermodynamics_kinetics/Precipitation-Simulation_CompuTherm.pdf)
- [54] ESTECO, modeFRONTIER (2017).  
URL <http://www.esteco.com/modefrontier>
- [55] R. Jha, N. Chakraborti, D. R. Diercks, A. P. Stebner, C. V. Ciobanu, DATA: Combined Machine Learning and CALPHAD Approach for Discovering Processing-Structure Relationships in Soft Magnetic Alloys, Citrine Informatics (2018).  
URL [https://citrination.com/datasets/154863/show\\_files](https://citrination.com/datasets/154863/show_files)
- [56] I. Sobol', On the distribution of points in a cube and the approximate evaluation of integrals, *USSR Computational Mathematics and Mathematical Physics* 7 (1967) 86–112.